

A doubly stochastic enhancement of the Failure Forecast Method using a noisy mean-reverting process

Andrea Bevilacqua¹, E. Bruce Pitman², Abani K. Patra^{3,4}, and Augusto Neri⁵

¹*Dept. of Earth Sciences, University at Buffalo, Buffalo, NY*

²*Dept. of Materials Design and Innovation, University at Buffalo, NY*

³*Dept. of Mech. and Aero. Eng., University at Buffalo, Buffalo, NY*

⁴*Comp. Data Science and Eng., University at Buffalo, Buffalo, NY*

⁵*Sezione di Pisa, Istituto Nazionale di Geofisica e Vulcanologia, Pisa, Italy*

{abevilac,pitman,abani}@buffalo.edu; augusto.neri@ingv.it

Abstract

We introduce a doubly stochastic method for performing material failure theory based forecasts of volcanic eruptions. The method enhances the well known Failure Forecast Method equation, introducing a new formulation similar to the Hull-White model. In particular, we incorporate a stochastic noise term in the original equation, and we extend the uncertainty quantification beyond previous efforts. The model is a stochastic differential equation (SDE) with a mean reverting solution, which assumes the traditional ordinary differential equation (ODE) as the mean solution. Our implementation allows the model to make excursions from the classical solutions, by including uncertainty in the estimation. The doubly stochastic formulation is particularly powerful, in that it provides a complete posterior probability distribution, allowing civil protection officials to determine a worst case scenario with a specified level of confidence. We validate the new method on historical datasets of precursory signals, across a wide range of possible values of convexity in the solutions and amounts of scattering in the observations. The results show the increased forecasting skill of the doubly stochastic formulation of the SDE.

Contents

1	Introduction	2
2	The Failure Forecast Method ODE	3
3	The Failure Forecast Method SDE	5
4	The mean-reverting properties	7
5	Parameter fitting and UQ	8
6	Examples of probability forecasts	13
7	Discussion	17
8	Conclusions	18
A	Classical statistical analysis of FFM	19
B	Sensitivity analysis on the noise properties	20

1 Introduction

The Failure Forecast Method (FFM) for volcanic eruptions is a classical tool in the interpretation of monitoring data as potential precursors, providing quantitative predictions of the eruption onset. The basis of FFM is a fundamental law for failing materials:

$$dX/dt = AX^\alpha,$$

where X is the rate of the precursor signal, and α , A are model parameters. The solution X is a power law of exponent $1/(1 - \alpha)$ diverging at time t_f , called failure time. The model represents the potential cascading of precursory signals leading to the final rupture of materials, with t_f a good approximation to the eruption onset time t_e .

The FFM equation was originally developed in landslide forecasting (Voight, 1987, 1988b; Voight et al., 1989), and later applied in eruption forecasting (Voight, 1988a, 1989; Cornelius and Voight, 1995). The method was retrospectively applied to several volcanic systems, including dome growth episodes and explosive volcanic eruptions (Voight and Cornelius, 1991; Cornelius and Voight, 1994, 1996; Voight et al., 2000). Volcanic tremor characteristics were studied with the FFM method and related to the seismic signals of the multi-scale rock cracking (Kilburn and Voight, 1998; Ortiz et al., 2003; Kilburn, 2003). Experimental and field studies of the physics behind the rate-increase of volcano-tectonic earthquakes are available (Smith et al., 2009; Smith and Kilburn, 2010). Generalized (power law) regression appeared to improve the accuracy of the forecasts (Bell et al., 2011). However, sometimes the method fails to predict the time of the eruption, and some volcanic systems are often characterized by prolonged unrest and ambiguous signals (Chiodini et al., 2016). A full probability assessment, including uncertainty quantification (UQ), is required, and it is the purpose of our investigations.

In this study, we generalize the classical FFM approach by incorporating a stochastic noise in the original ordinary differential equation (ODE) converting it into a stochastic differential equation (SDE), and systematically characterizing the uncertainty. Embedding noise in the model can enable the FFM equation to have greater forecasting skill by focusing on averages and moments. Sudden changes in the power law properties are indeed possible. In our model, the prediction is thus perturbed inside a range that can be tuned, producing probabilistic forecasts.

In more detail, in the original equation the change of variables $\eta = X^{1-\alpha}$ implies:

$$d\eta/dt = (1 - \alpha)A,$$

i.e. a straight line which hits zero at t_f . The most efficient graphical and computational methods indeed rely on the regression analysis of inverse rate plots. We re-define η with:

$$d\eta_t = \gamma[(1 - \alpha)A(t - t_0) + \eta_{t_0} - \eta_t]dt + \sigma dWt,$$

also called Hull-White model in financial mathematics (Hull and White, 1990). The parameter σ defines the strength of the noise, and γ the rapidity of the mean-reversion property. We validate the new method on historical datasets of precursory signals already studied with the classical FFM, including tilt, line-length, and fault movement at Mt. St. Helens, 1981-82, seismic signals registered from Bezmyanny, 1960, and surface movement of Mt. Toc, 1960-63 (Voight, 1988a).

A fundamental aspect of our formulation is the possibility of a doubly stochastic UQ. Doubly stochastic models describe the effect of uncertainty in the formulation of aleatory processes, and have been successfully applied in volcanology (Sparks and Aspinall, 2004; Marzocchi and Bebbington, 2012; Bevilacqua, 2016). Thus, doubly stochastic probability density functions (pdf) and estimates are themselves affected by uncertainty. This approach has been applied in spatial problems concerning eruptive vent/fissure mapping (Selva et al., 2012; Bevilacqua et al., 2015; Tadini et al., 2017b,a; Bevilacqua et al., 2017a), long-term temporal problems based on past eruption record (Bebbington, 2013; Bevilacqua et al., 2016; Richardson et al., 2017; Bevilacqua et al., 2018), and hazard assessments (Neri et al., 2015; Bevilacqua et al., 2017b). In this study, a doubly stochastic model is applied in a short-term eruption forecasting method based on precursory signals.

2 The Failure Forecast Method ODE

The classical Failure Forecast Method (FFM) equation is:

$$\dot{\Omega}^{-\alpha}\ddot{\Omega} = A, \quad (1)$$

where $\alpha \geq 1$, $A > 0$, and $\Omega : [0, T] \rightarrow \mathbb{R}$ a precursor function, like ground or fault displacement, tilt, seismic strain release (Voight, 1988a). For simplicity we call $X := \dot{\Omega}$, and the equation 1 reads:

$$X^{-\alpha} \frac{dX}{dt} = A.$$

If $\alpha = 1$, the solution is the exponential $X(t) = X(t_0) \exp[A(t - t_0)]$. However, most common observations in volcanology give $\alpha \in [1.7, 2.3]$. We note that if $\alpha < 1$ a solution exists in $[0, +\infty]$ and does not diverge in a finite time (Cornelius and Voight, 1995).

If $\alpha > 1$, we see:

$$\frac{dX^{1-\alpha}}{dt} = (1-\alpha)X^{-\alpha} \frac{dX}{dt},$$

and the FFM equation becomes:

$$\frac{dX^{1-\alpha}}{dt} = (1-\alpha)A.$$

Simplifying again the notation, we can call $\eta = X^{1-\alpha}$, and the FFM reads:

$$\frac{d\eta}{dt} = (1-\alpha)A.$$

We can solve this equation by immediate integration,

$$\eta(t) = (1-\alpha)A(t - t_0) + \eta(t_0), \quad (2)$$

and equivalently:

$$X(t) = [(1-\alpha)A(t - t_0) + X(t_0)^{1-\alpha}]^{\frac{1}{1-\alpha}}. \quad (3)$$

The original method required fitting the two parameters α and A on the monitoring data, and then to estimate the time of failure t_f , such that $X(t_f) = +\infty$, or equivalently $\eta(t_f) = 0$. It follows:

$$\eta(t) = (\alpha - 1)A(t_f - t),$$

and so:

$$t_f - t = \frac{\eta(t)}{(\alpha - 1)A}.$$

We note that an estimate of $\eta(t)$ is thus necessary to make forecasts, a non-trivial process if noise is present.

The effect of varying parameters α and A in the equation 3 is displayed in Figure 1a,b. Our purpose is to forecast the failure time $t_f := \{t : X(t)^{-1} = 0\}$ and hence it is more practical to examine the plot of $X^{-1} = \eta^{\frac{1}{\alpha-1}}$, shown in Fig.1b. The parameter α defines the convexity of that function - for $\alpha \leq 2$ it is convex, for $\alpha \geq 2$ it is concave. The value $\alpha = 2$ produces a straight line. We call it the *convexity* parameter.

In equation 2 the parameter A changes the time scale of the equation, and so defines the constant slope of η , that is $-A$. Hence we call it the *slope* parameter.

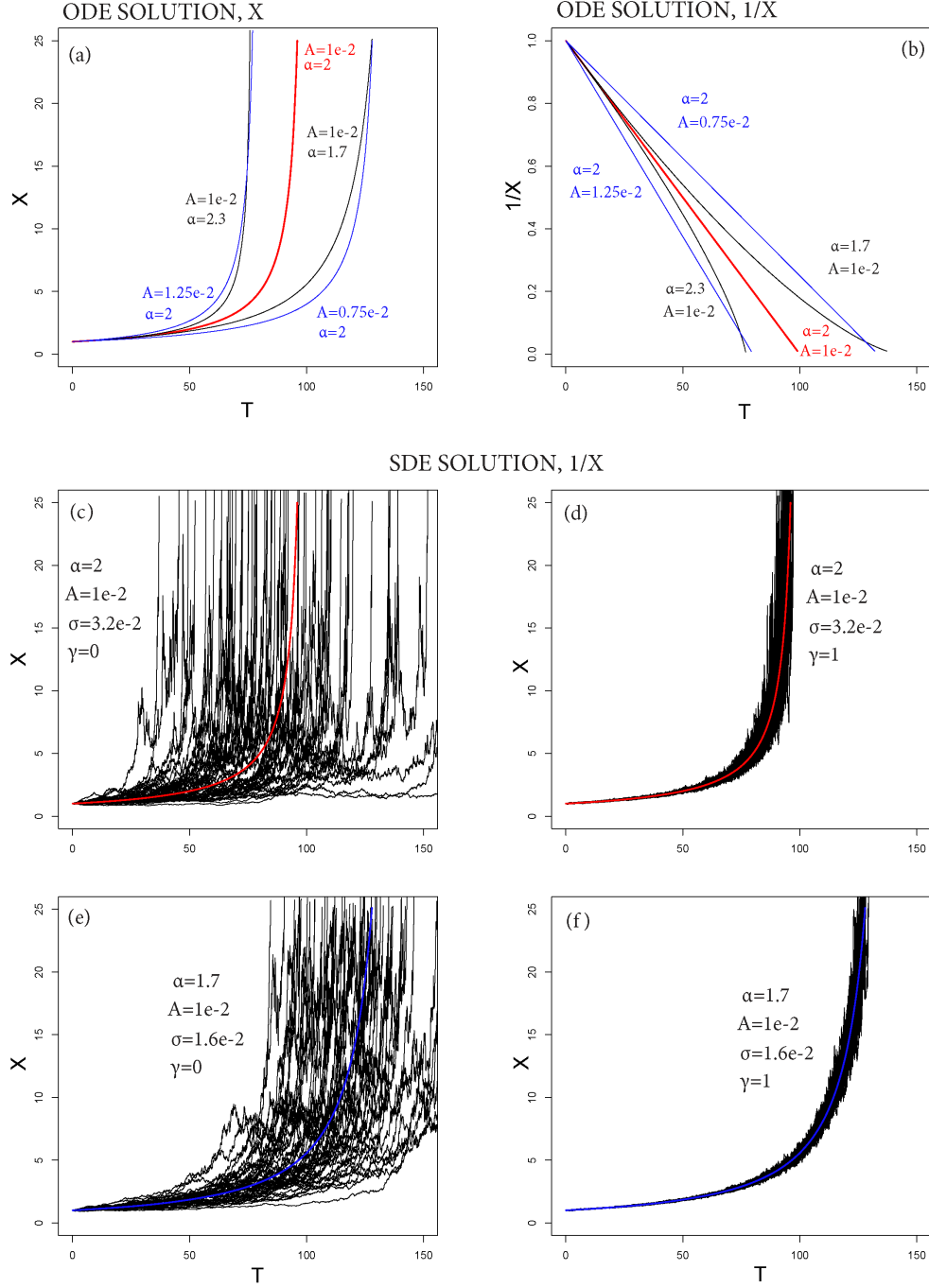


Figure 1: (a,b) ODE solution, (a) X , and (b) $1/X$. (c-f) SDE solution, (c,e) with $\gamma = 0$, (d,f) with $\gamma = 1$. (c,d) with $\alpha = 2$, (e,f) with $\alpha = 1.7$. In all the plots, the colored lines are the ODE solutions, the black lines are 50 random paths of the SDE solutions.

3 The Failure Forecast Method SDE

We assume that the equation is not exactly verified, but there is a transient difference, which however decreases exponentially through time. The equation becomes:

$$\eta(t) = (1 - \alpha)A(t - t_0) + \beta \exp(-\gamma t) + \eta(t_0),$$

where β is the value at $t = 0$ and γ is the rate of decay of this error term.

This allows a reformulation of the equation. Given that:

$$\eta(t) - (1 - \alpha)A(t - t_0) - \eta(t_0) = \beta \exp(-\gamma t),$$

then

$$\ln [\eta(t) - (1 - \alpha)A(t - t_0) - \eta(t_0)] = -\gamma t + \ln(\beta).$$

We can take the derivative, and obtain:

$$[\eta(t) - (1 - \alpha)A(t - t_0) - \eta(t_0)]^{-1} \left(\frac{d\eta}{dt}(t) - (1 - \alpha)A \right) = -\gamma,$$

and so

$$\frac{d\eta}{dt} = \gamma [(1 - \alpha)A(t - t_0) + \eta(t_0) - \eta(t)] + (1 - \alpha)A.$$

In addition, we want to allow for an additive noise affecting the new equation, and the final formulation is:

$$d\eta_t = \{\gamma [(1 - \alpha)A(t - t_0) + \eta_{t_0} - \eta_t] + (1 - \alpha)A\} dt + \sigma dW_t, \quad (4)$$

or equivalently:

$$X_t = \left\{ X_{t_0}^{1-\alpha} + \int_{t_0}^t \{\gamma [(1 - \alpha)A(s - t_0) + X_{t_0}^{1-\alpha} - X_s^{1-\alpha}] + (1 - \alpha)A\} ds + \int_{t_0}^t \sigma dW_s \right\}^{\frac{1}{1-\alpha}}, \quad (5)$$

for each $t < t_f$. This is also called a Hull-White model in financial mathematics (Hull and White, 1990).

The effect of varying parameters σ and γ on the SDE solution X is displayed in Figure 1c-f. In equation 4, σ defines the time scale of the additive noise, and so we call it the *noise* parameter. We remark that X is nonlinearly affected by this random noise in equation 5. The SDE defining η is elevated to the exponent $\frac{1}{1-\alpha}$, and even a relatively small noise can significantly change the failure time (see Fig.1c,e).

Parameter γ defines the time scale of the exponential decay of perturbations with respect to the classical ODE solution. It controls the equation, reverting the paths of the solutions towards the mean curve (see Fig.1d,f). We call γ the *mean-reverting* parameter.

Figure 2 displays three different solutions of X^{-1} , assuming convexity parameter $\alpha = 1.7, 2$, or 2.3 . The slope parameter is fixed $A = 1e - 1$. Plots 2a,c,e show an example of solutions assuming mean-reverting parameter $\gamma = 0$, or $\gamma = 0.25$. The noise is additive in 2a, and weakly nonlinear in 2c,e. Plots 2b,d,f display pdf of t_f calculated by Monte Carlo simulation (2,000 samples).

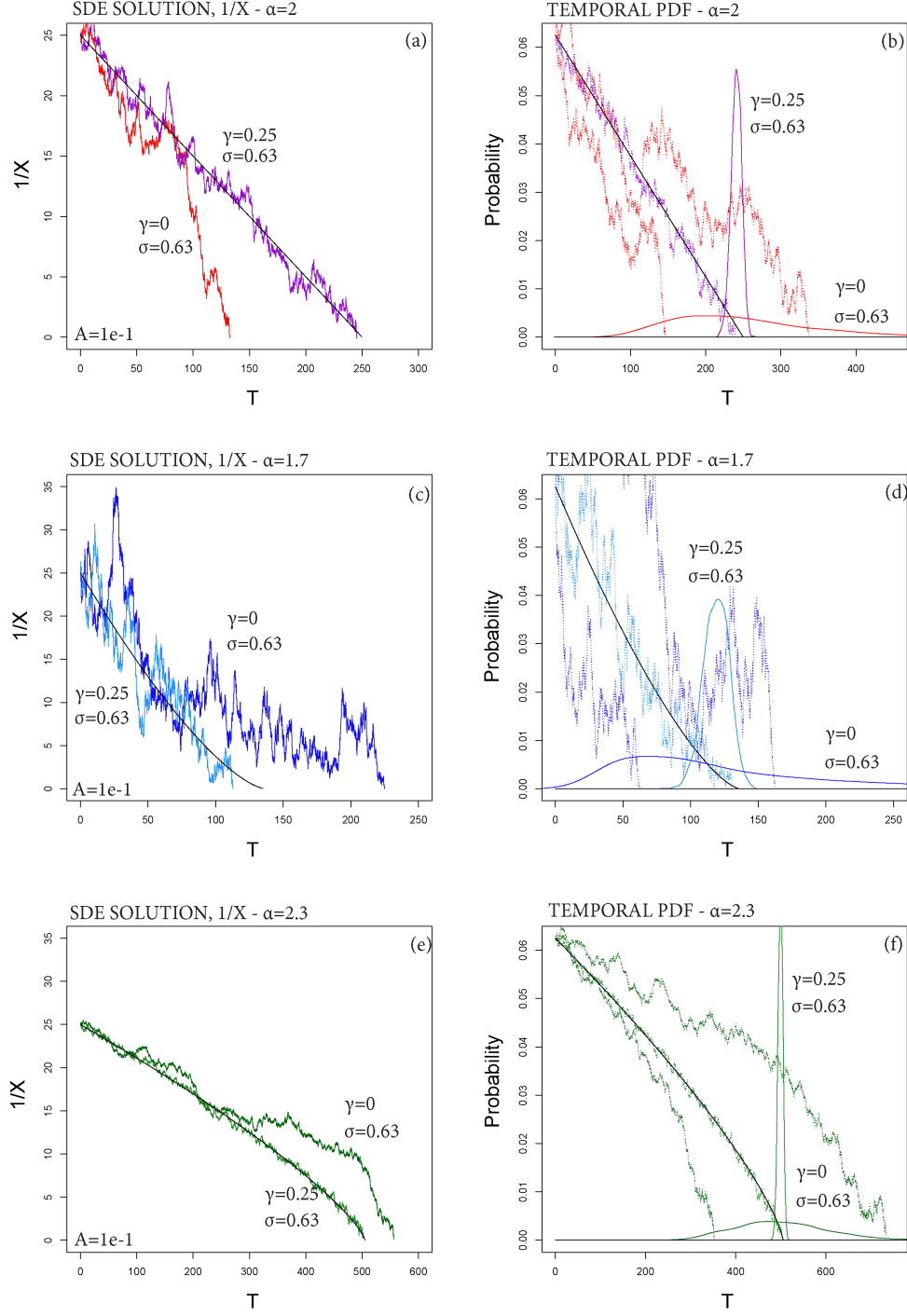


Figure 2: SDE solutions, $1/X$, (a,b) with $\alpha = 2$, (c,d) with $\alpha = 1.7$, (e,f) with $\alpha = 2.3$. In (a,c,e) the colored lines are random paths of the solution, assuming $\gamma = 0$ or $\gamma = 0.25$. In (b,d,f) the colored lines are the pdfs of t_f , assuming $\gamma = 0$ or $\gamma = 0.25$. The dotted lines are random paths of the solution. In all the plots the black line is the ODE solution.

4 The mean-reverting properties

Let $\hat{\eta}$ be the ODE solution with data $\eta(t_0)$ at time t_0 . If $\sigma > 0$ and $\gamma = 0$, the law of Brownian Motion and the linearity of the ODE imply that:

$$\eta(t) - \hat{\eta}(t) \sim \mathcal{N}(0, \sigma^2(t - t_0)).$$

If $\gamma > 0$ the *mean-reverting* term exponentially reduces $|\eta(t) - \hat{\eta}(t)|$. If $\sigma = 0$ and the equation starts with $\delta(t_0) := |\eta(t_0) - \hat{\eta}(t_0)| > 0$ we have:

$$\delta(t) := |\eta(t) - \hat{\eta}(t)| = \exp[-\gamma(t - t_0)].$$

Figure 3a shows this example, and $3\gamma^{-1}$ provides the time interval required to have $\delta(t) \simeq \delta(t_0)/20$.

If both $\sigma > 0$ and $\gamma > 0$, the combined effect of the *noise* and the *mean-reverting* defines the Ornstein-Uhlenbeck process (from equation 4, with $A = 0$ and $\eta_{t_0} = 0$):

$$d\eta_t = -\gamma\eta_t dt + \sigma dW_t, \quad (6)$$

whose solution is:

$$\eta_t \sim \mathcal{N}\left(0, \frac{\sigma^2}{2\gamma} [1 - \exp(-2\gamma t)]\right) \simeq \mathcal{N}\left(0, \frac{\sigma^2}{2\gamma}\right), \quad (7)$$

when $\gamma|t_f - t_0| \gg 1$. The constant $K := \frac{\sigma^2}{2\gamma}$ uniquely defines the probability distribution of the solution of this SDE. Different realizations of this process are displayed in in Figure 3b. If σ^2 increases and γ decreases, then the perturbations are more frequent, but reverted faster. This may have some effect on the estimate of t_f , but discrete data cannot provide any information on perturbations occurred at frequency higher than the measurements. In most of our examples we define $\gamma^{-1} = 15$ days. That is, any perturbation decays by 63% within 15 days, and by 95% within 45 days, which is close to the total length of the time interval considered. Sensitivity analysis on this parameter is performed in Appendix B.

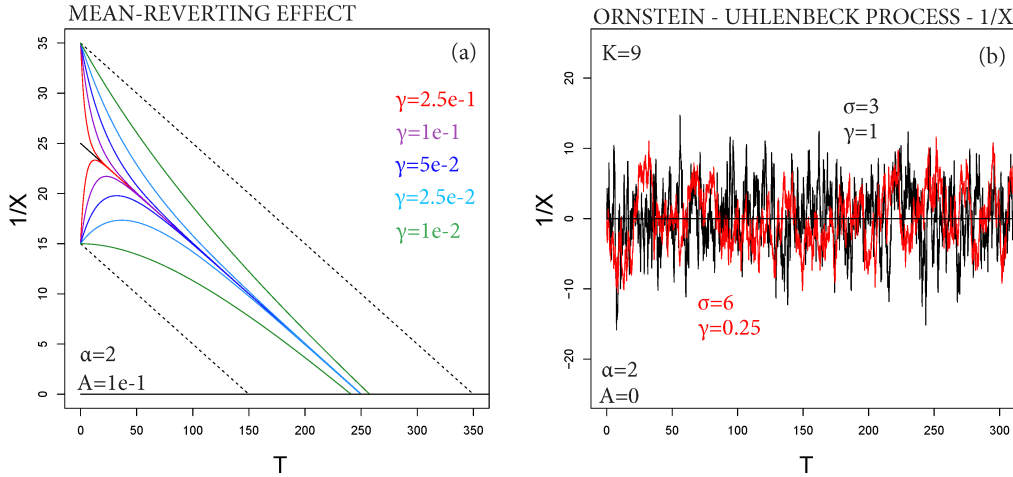


Figure 3: (a) SDE solutions with $\alpha = 2$, $1/X$, with $\sigma = 0$, but $\delta(t_0) > 0$. Different colors correspond to different values of γ . (b) Ornstein-Uhlenbeck processes with equal $K = \frac{\sigma^2}{\gamma}$, but different (σ, γ) .

5 Parameter fitting and UQ

The application of our method requires the estimation of five parameters:

- *curvature* parameter α ,
- *slope* parameter A ,
- *noise* parameter σ ,
- *mean-reverting* parameter γ ,
- an unperturbed initial value $\hat{\eta}(t_0)$.

In the following all these parameters are assumed to be positive, and $\alpha > 1$. In particular, the case $\alpha = 1$ is trivial, and the cases $\alpha < 1$ or $A \leq 0$ imply $t_f = +\infty$. We note that $\hat{\eta}(t_0)$ cannot be trivially defined equal to the first observation, because of the perturbations.

Several methods have been adopted in the determination of the parameters in the ODE problem (Voight, 1988a; Cornelius and Voight, 1995; Bell et al., 2011). The Log-rate versus Log-acceleration Technique (LLT), and the Hindsight Technique (HT) can both provide estimates of α . They are described in Appendix A. The first technique is generally less accurate because needs an estimate of the time derivative of the observations. The second technique requires that we know t_e and hence can only be used in retrospective analysis (hindcasting problems). In our formulation we use these methods in the estimation of α . The ODE represents the mean path of the SDE, and we approximate its curvature from the available observations.

If α is given, a linearized least square method (LLSM) can be applied to fit parameter A and $\hat{\eta}(t_0)$ on the inverse plot $1/X$. This is the main method classically adopted as a forecasting technique in the ODE problem (see Appendix A). We fit the stochastic parameters σ and γ from the residuals of this linearized problem. In particular, we impose the constant $K = \frac{\sigma^2}{2\gamma}$ to be equal to the variance of the residuals. In summary, we plug-in α from classical LLT or HT in the LLSM, and then we obtain $(A, \hat{\eta}(t_0), K)$ as required to the SDE definition.

We apply three different forecast methods on the datasets in Voight (1988a), and we test t_f as an estimator of t_e . In all our methods t_f is assumed as a random variable, and its pdf

$$g_{t_f} : \mathbb{R} \rightarrow \mathbb{R}+, \quad \int_0^\infty g_{t_f}(x)dx = 1$$

is estimated following a classical Gaussian kde method (Silverman Rule).

- Method 1 is based on the classical ODE, and the corresponding forecasts are displayed in Figure 4. This is consistent with the original formulation in Voight (1988a). g_{t_f} depends on the statistical uncertainty affecting the pair $(A, \hat{\eta}(t_0))$ in the regression method. We implement this *model uncertainty* as a bivariate Gaussian in a Monte Carlo of 5,000 samples.

Methods 2 and 3 are both based on the new SDE.

- In Method 2, the least-square curve is assumed to be the mean solution, and g_{t_f} is defined by the noise. The forecasts are displayed in Figure 5. We implement this *aleatory uncertainty* in a Monte Carlo of 5,000 sample paths of the stochastic noise.
- Method 3 is *doubly stochastic* (e.g. Bevilacqua (2016)). The mean solution is affected first by the statistical uncertainty in the regression method, and then perturbed by the stochastic noise. The values of g_{t_f} are thus reported as 5th percentile, mean, and 95th percentile curves. We remark that the two uncertainties are not independent, because the properties of the noise are related to the residuals in the linearized problem. The forecasts are displayed in Figure 6. In this case, the mean pdf is based on a Monte Carlo sampling consisting of 10,000 model runs, while the percentile values are based on a hierarchical Monte Carlo of a variable number of samples. This number is tuned according to the different convergence rates observed, but is always above $200 \times 300 = 6e5$ samples.

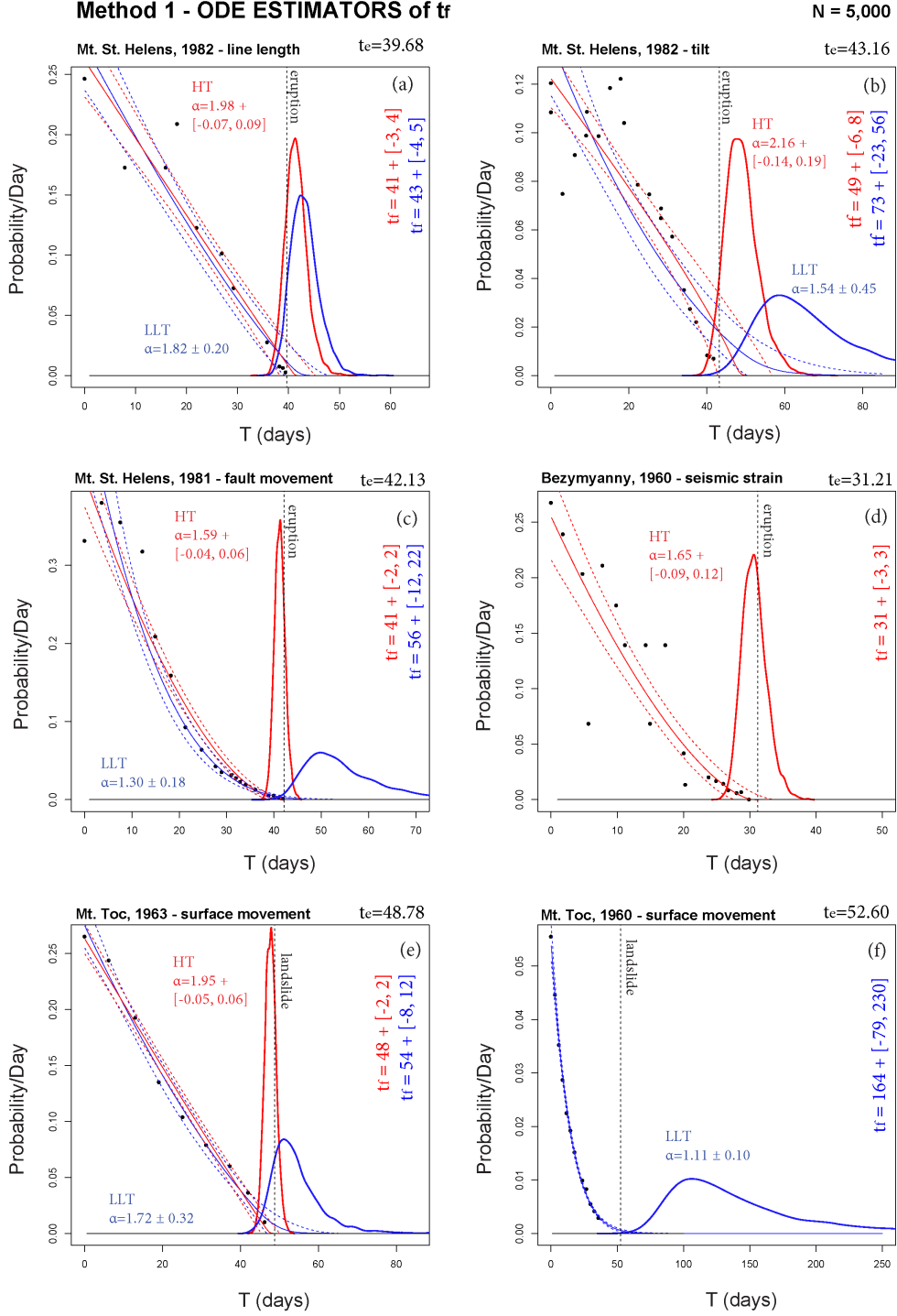


Figure 4: Estimators of t_f based on Method 1. Blue lines assume α as from LLT, red as from HT. The bold line is g_{t_f} . Thin dashed lines bound the 90% confidence interval of the ODE paths, and a thin continuous line is the mean path. A dashed black line marks t_e . Method 1 generally provides a good estimator of t_e , but often only the HT method allows these robust estimates.

Method 2 - SDE ESTIMATORS of t_f

N = 5,000

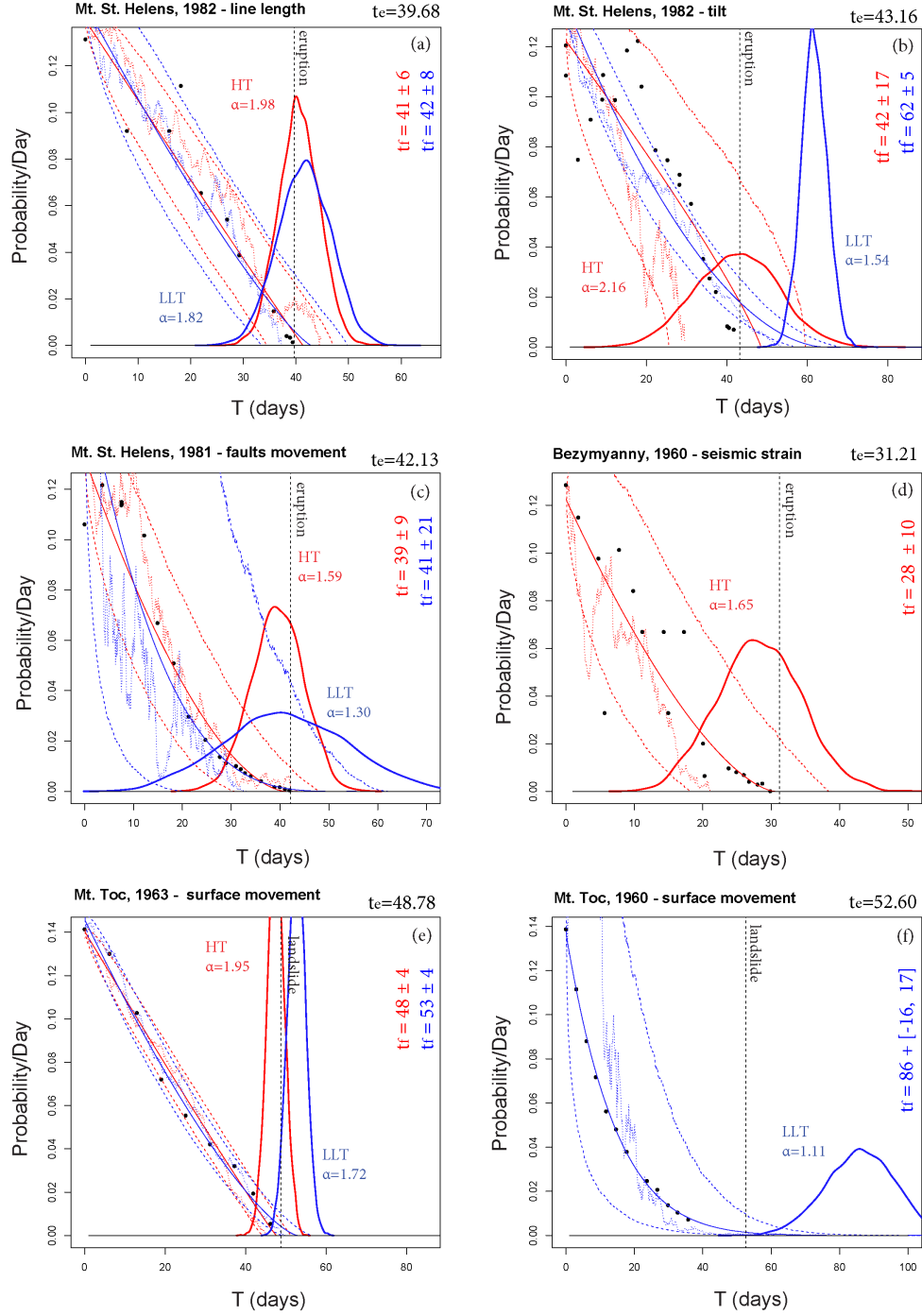


Figure 5: Estimators of t_f based on Method 2. Blue lines assume α as from LLT, red as from HT. A bold line is g_{t_f} . Thin dashed lines bound the 90% confidence interval of the SDE paths, and a thin continuous line is the mean path. Thin dotted lines show examples of random paths. A dashed black line marks t_e . Method 2 reduces the overestimation issues of Method 1, but model uncertainty is neglected and the estimates can miss t_e .

Method 3 - DOUBLY STOCHASTIC ESTIMATORS of t_f

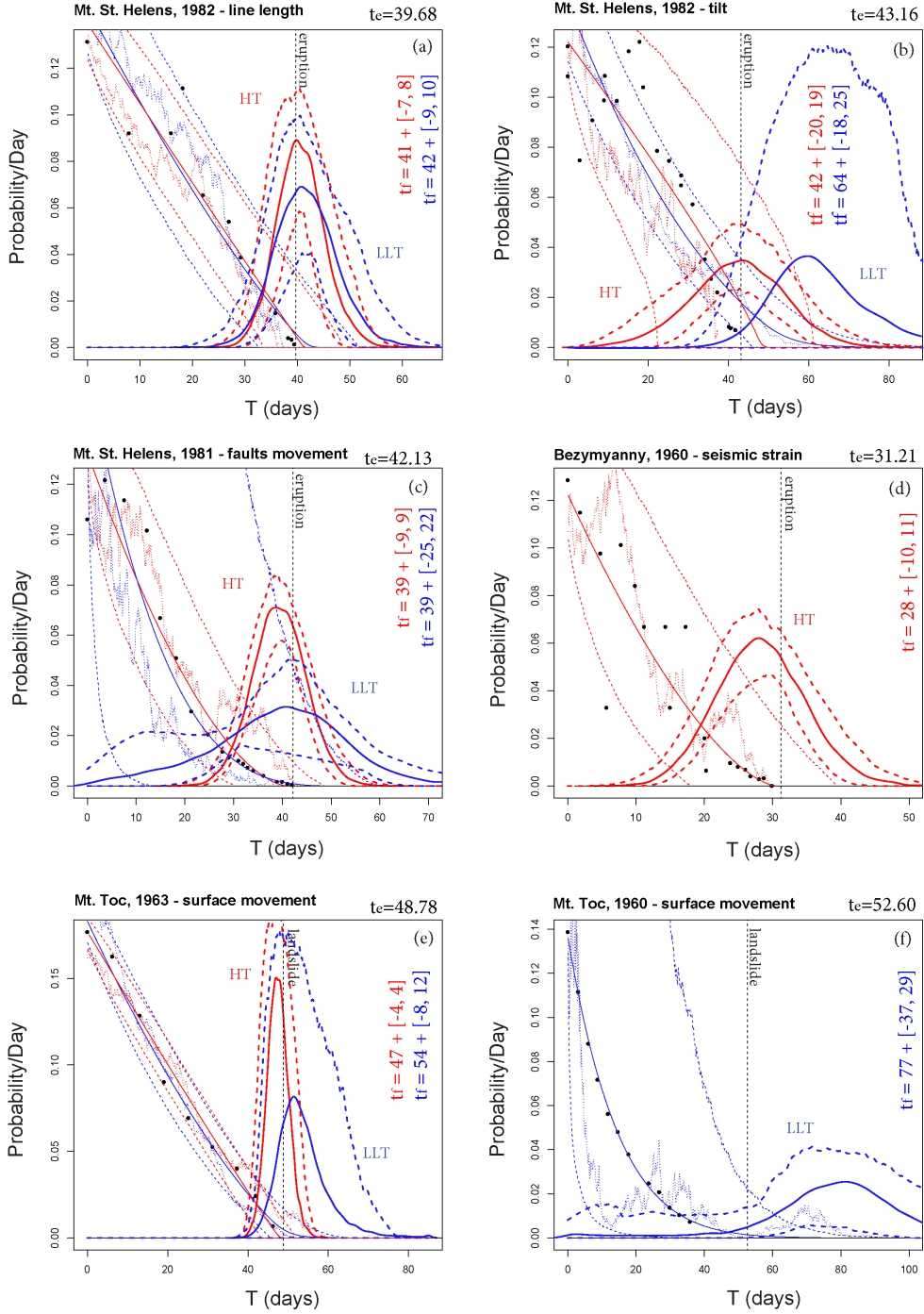


Figure 6: Estimators of t_f based on Method 3. Blue lines assume α as from LLT, red as from HT. A bold line is g_{t_f} , and bold dashed lines are its 5th and 95th percentile values. Thin dashed lines bound the 90% confidence interval of the SDE paths, and a thin continuous line is the mean path. Thin dotted lines show examples of random paths. A dashed black line marks t_e . Method 3 enhances Method 2 and performs significantly better.

The six case studies refer to the volcanic eruptions of Mt. St. Helens (USA), 1982 (a,b) and 1981 (c), and of Bezymyanny (USSR), 1960 (d), and to the landslides of Mt. Toc (Italy), 1960 (e) and 1963 (f). These datasets are characterized by different values of α , and by different confidence intervals in the linear regression. Estimates of α are based on data reported in Appendix A.

In general, the mean path is consistent in the three methods, but UQ is significantly different, as well as the values of g_{t_f} . In particular:

- (a) **Mt. St. Helens, 1982 - line length** data values are initially scattered, until $t = t_e - 20$, and then become more aligned. $\alpha \approx 2$, and $E[t_f]$ overestimates t_e of 2-3 days in all the Methods. Uncertainty range is 50% larger in Method 2 and 3 compared to Method 1.
- (b) **Mt. St. Helens, 1982 - tilt** this example refers to the same eruption of example (a), but the dataset is larger. The number of initially scattered data is relatively significant. According to HT, $\alpha = 2.2 \pm 0.2$, while according to LLT $\alpha = 1.5 \pm 0.5$. In the first case (red), in Method 1 $E[t_f]$ overestimates t_e of 6 days, and in Method 2 and 3 it underestimates t_e of only 1 day. Uncertainty range is about ± 7 days in Method 1, and about ± 20 days in Methods 2 and 3. In the second case (blue), in Method 1 $E[t_f]$ misses t_e of 30 days, outside the uncertainty range. In Method 2 and 3 $E[t_f]$ overestimates t_e of 20 days, and has a relatively small uncertainty range of ± 5 days which misses t_e . Method 3 is slightly improved, and almost captures t_e in its uncertainty range.
- (c) **Mt. St. Helens, 1981 - fault movement** this example is characterized by $\alpha \approx 1.6$ in HT and $\alpha = 1.3 \pm 0.2$ in LLT. In the first case (red), in Method 1 $E[t_f]$ underestimates t_e of only 1 day, with uncertainty range ± 2 days. Methods 2 and 3 also perform well, but uncertainty ranges increase to ± 9 . In the second case (blue), in Method 1 $E[t_f]$ overestimates t_e of 14 days, outside the uncertainty range. In Methods 2 and 3, $E[t_f]$ is 1 and 3 days before t_e , respectively. The uncertainty is above ± 20 days.
- (d) **Bezymyanny, 1960 - seismic strain** data values are persistently scattered until $t = t_e - 10$, and $\alpha \approx 1.6$. However, in Method 1, $E[t_f]$ correctly estimates t_e , with uncertainty range of ± 3 days. In Methods 2 and 3, $E[t_f]$ underestimates t_e of 3 days, and uncertainty is increased to ± 9 days.
- (e) **Mt. Toc, 1963 - surface movement** According to HT, $\alpha \approx 2$, while according to LLT, $\alpha = 1.7 \pm 0.3$. In the first case (red), in Method 1 $E[t_f]$ correctly estimates t_e , with uncertainty range of ± 2 days. Similar performances in Method 2 and 3, with uncertainty range of ± 4 days. In the second case (blue), in Method 1 $E[t_f]$ overestimates t_e of 5 days, but the uncertainty range is about ± 10 days and captures it. In Method 2 $E[t_f]$ overestimates t_e of 4 days and uncertainty is reduced to ± 4 days. Method 3 gives very similar results to Method 1.
- (f) **Mt. Toc, 1960 - surface movement** this example is characterized by a very low $\alpha \approx 1.1$. Even if data are not significantly scattered, uncertainty is very high because the ODE solutions are almost asymptotical to the real axis. In Method 1, $E[t_f]$ significantly overestimates t_e of more than 100 days, and uncertainty range is at the same scale. In Method 2, $E[t_f]$ overestimates t_e of 34 days, and uncertainty range is reduced to ± 16 days. In Method 3, $E[t_f]$ overestimates t_e of 25 days, and the uncertainty range is about ± 35 days, capturing t_e .

In summary, when $\alpha \approx 2$ Method 1 generally provides a good estimator of t_e , but often only the HT method allows these robust estimates. Instead, when $\alpha \leq 1.6$, Method 1 tends to overestimate t_e . Method 2 reduces this issue, but model uncertainty is neglected and the estimate can miss t_e . Method 3 enhances Method 2, and performs significantly better in this case. Its doubly stochastic nature allows the production of either mean probability values or more conservative 95th percentile values.

6 Examples of probability forecasts

The estimators defined in the previous section are informed by the entire sequence of data, up to the eruption onset or landslide initiation t_e . This provides useful insight on the validity of the estimators, but it is not a forecast. Indeed in any forecasting problem the sequence of data is available up to a time $t_1 < t_e$, that represents the current time of the forecast. All the data collected after time t_1 cannot be considered.

In the following figures we display forecasts of t_e based on the ODE method, and obtained considering only the data collected in limited time windows $T = [t_2, t_1]$. We focus on the two examples of (i) Mt. St. Helens, 1982 - line length ($\alpha \approx 1.98$), and (ii) Bezymyanny, 1960 - seismic strain ($\alpha \approx 1.65$). Figure 7 adopts Method 1, Figure 8 Method 2 and Figure 9 Method 3. Method 1 and mean pdf in Method 3 both implement a Monte Carlo of 20,000 samples, Method 2 a Monte Carlo of 5,000 samples, the percentile values in Method 3 are based on a hierarchical Monte Carlo of more than $6e5$ samples.

Forecasting problems are significantly uncertain, because they are inherently extrapolations based on past data. In Methods 1 and 3, sometimes $P\{t_f = \infty\} > 0$ and there is a non-negligible chance that the solution path never hits the real axis. In contrast, if $P\{t_f < t_1\} > 0$ there is a chance that $\hat{\eta}(t_1) < 0$ and the equation is not well defined. The probability of both these events is quantified.

In both examples we consider three time windows progressively moving towards t_e , including new observations and neglecting the old data. In particular, (a-b) rely on the initial scattered data, (c-d) include both scattered and aligned observations, (e-f) generally forget about scattered data. We remark that α remains fixed for simplicity.

In general, uncertainty is always reduced while getting closer to t_e . In particular:

- (a) **Mt. St. Helens, 1982 - line length** Based on the first time window (blue) $t_e - [40, 20]$, in Method 1 $E[t_f]$ overestimates t_e of 90 days, at the boundary of the uncertainty range. In Method 2 $E[t_f]$ overestimates t_e of 48 days, outside the uncertainty range. In Method 3 $E[t_f]$ overestimates t_e of 57 days, inside the uncertainty range. In Methods 1 and 3, $P\{t_f = \infty\} > 15\%$. Based on the second time window (light blue) $t_e - [40, 15]$, in Method 1 $E[t_f]$ overestimates t_e of 37 days, inside the uncertainty range. In Method 2 $E[t_f]$ overestimates t_e of 28 days, again outside the uncertainty range. In Method 3 $E[t_f]$ overestimates t_e of 30 days, inside the uncertainty range. In Methods 1 and 3, $P\{t_f = \infty\} \approx 2\%$. Based on the third time window (red) $t_e - [30, 10]$, in Method 1 $E[t_f]$ estimates correctly t_e , with an uncertainty range of about ± 8 days. In Method 2 $E[t_f]$ underestimates t_e of 1 day, with an uncertainty range of about ± 4 days. Method 3 performs similarly to Method 1.
- (d) **Bezymyanny, 1960 - seismic strain** This example is characterized by uncertainty ranges generally skewed towards higher values. Based on the first time window (blue) $t_e - [37, 17]$, in Method 1 $E[t_f]$ overestimates t_e of 21 days, inside the uncertainty range. In Method 2 $E[t_f]$ overestimates t_e of 1 day. In Method 3 $E[t_f]$ overestimates t_e of 5 days, well inside the uncertainty range. In Methods 1 and 3, $P\{t_f = \infty\} \approx 9\%$. Based on the second time window (light blue) $t_e - [30, 10]$, in Method 1 $E[t_f]$ overestimates t_e of 3 days, inside the uncertainty range. In Method 2 $E[t_f]$ underestimates t_e of 1 day, uncertainty $[-7, 11]$ days. In Method 3 $E[t_f]$ estimates t_e correctly, uncertainty of $[-8, 17]$ days. Based on the third time window (violet) $t_e - [20, 5]$, in Method 1 $E[t_f]$ underestimates t_e of 1 day, uncertainty of $[-3, 6]$ days. In Method 2 $E[t_f]$ underestimates t_e of 3 days, uncertainty range of about $[-2, 3]$ days. Method 3 performs similarly to Method 1. We remark that in Methods 1 and 3, $P\{t_f < t_1\} \approx 15\%$.

In summary, Method 1 and Method 3 give similar results, but the more complex UQ related to Method 3 improves its performance, particularly when uncertainty is large. Method 2 tends to give a competitive forecast only when the eruption is close, and model uncertainty is generally reduced. The doubly stochastic formulation of Method 3 appears to have a significant impact.

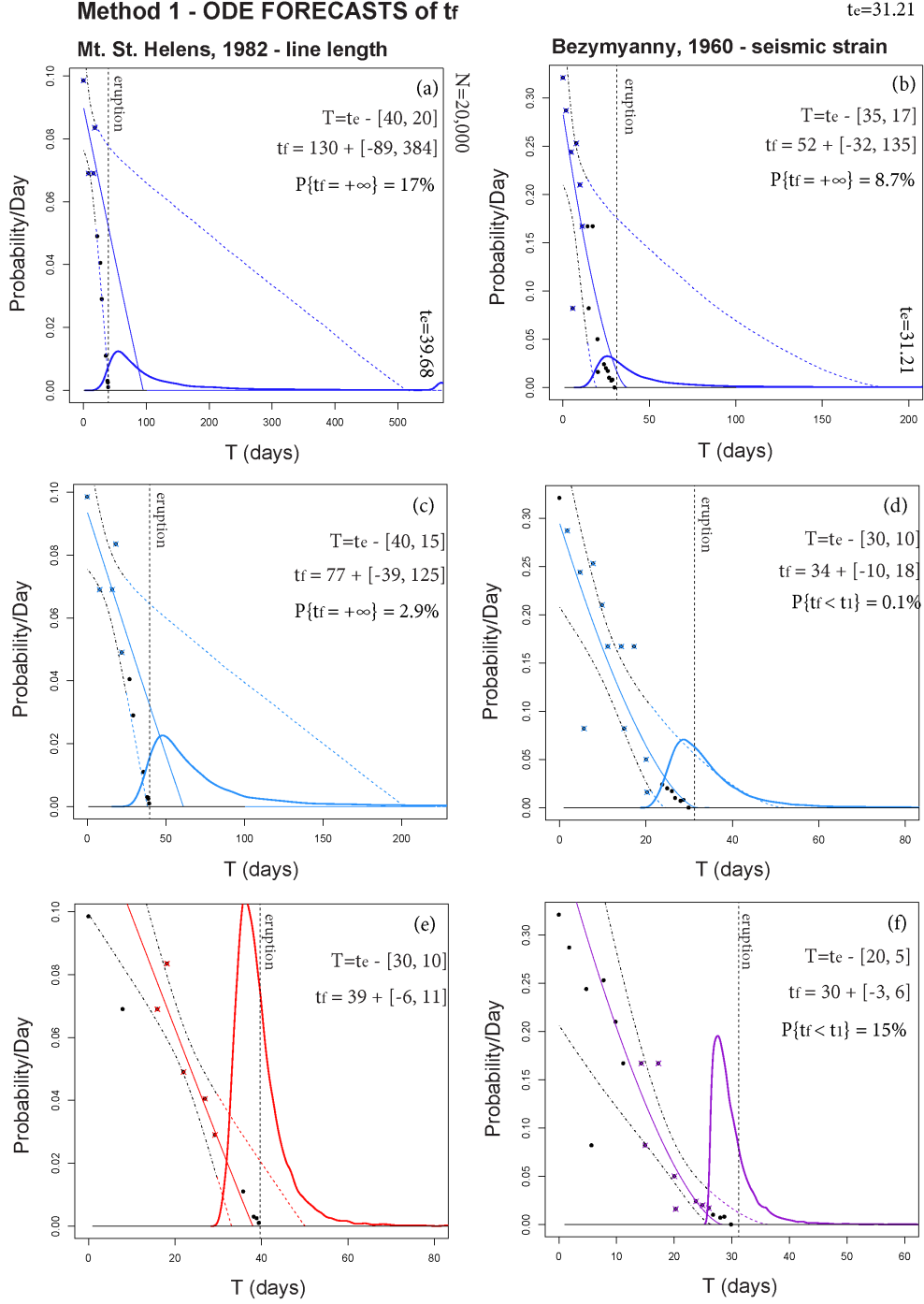


Figure 7: Forecasts of t_f based on Method 1. In (a,c,e) and (b,d,f) two examples are tested on three different time windows T . The bold line is g_{t_f} . Thin dashed lines bound the 90% confidence interval of the ODE paths, and a thin continuous line is the mean path. A dashed black line marks t_e .

Method 2 - SDE FORECASTS of t_f

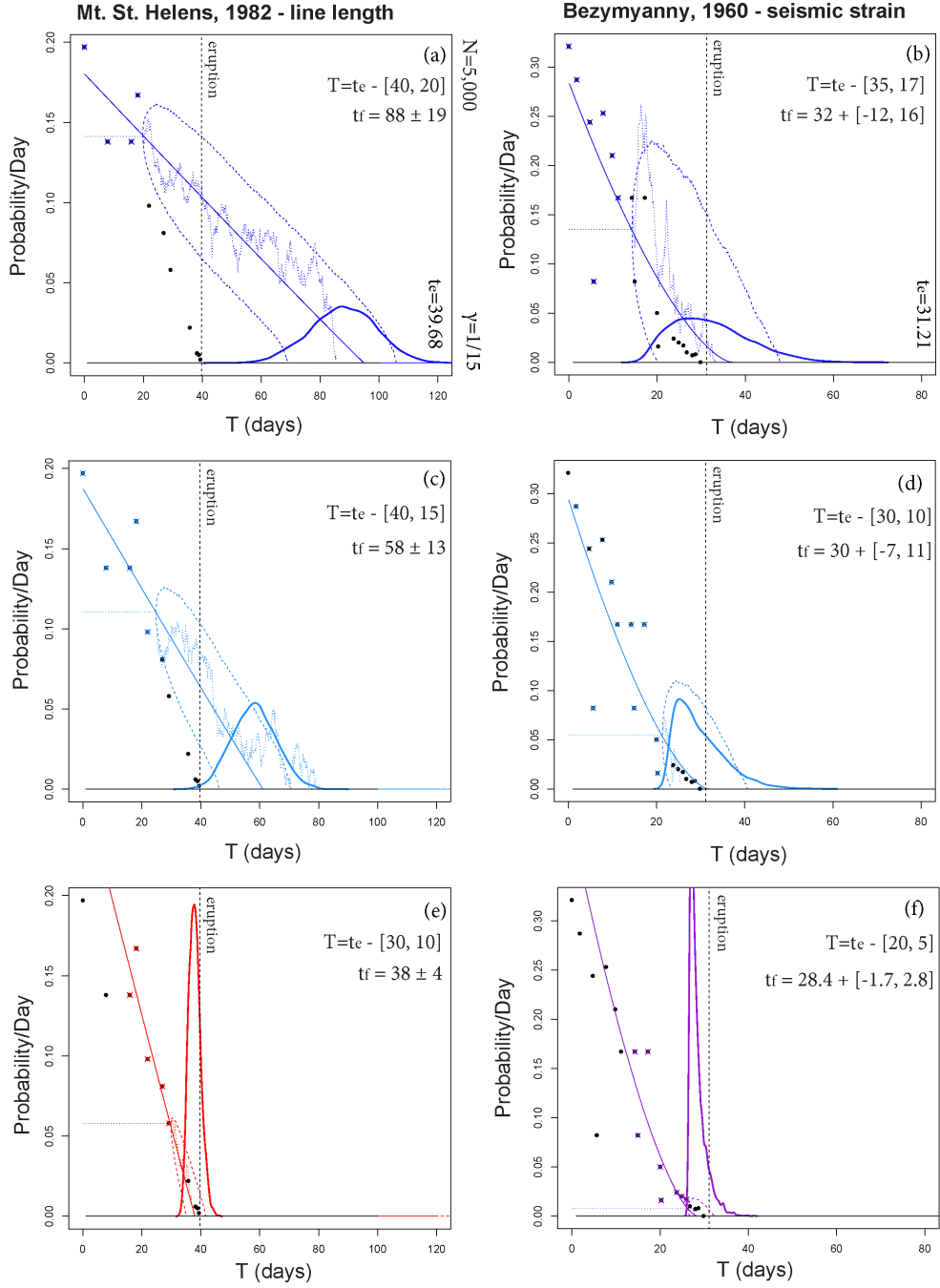


Figure 8: Forecasts of t_f based on Method 2. In (a,c,e) and (b,d,f) two examples are tested on three different time windows T . The bold line is g_{t_f} . Thin dashed lines bound the 90% confidence interval of the SDE paths, and a thin continuous line is the mean path. Thin dotted lines show examples of random paths. A thin dashed line marks $1/x_0$, and a dashed black line marks t_e .

Method 3 - DOUBLY STOCHASTIC FORECASTS of t_f

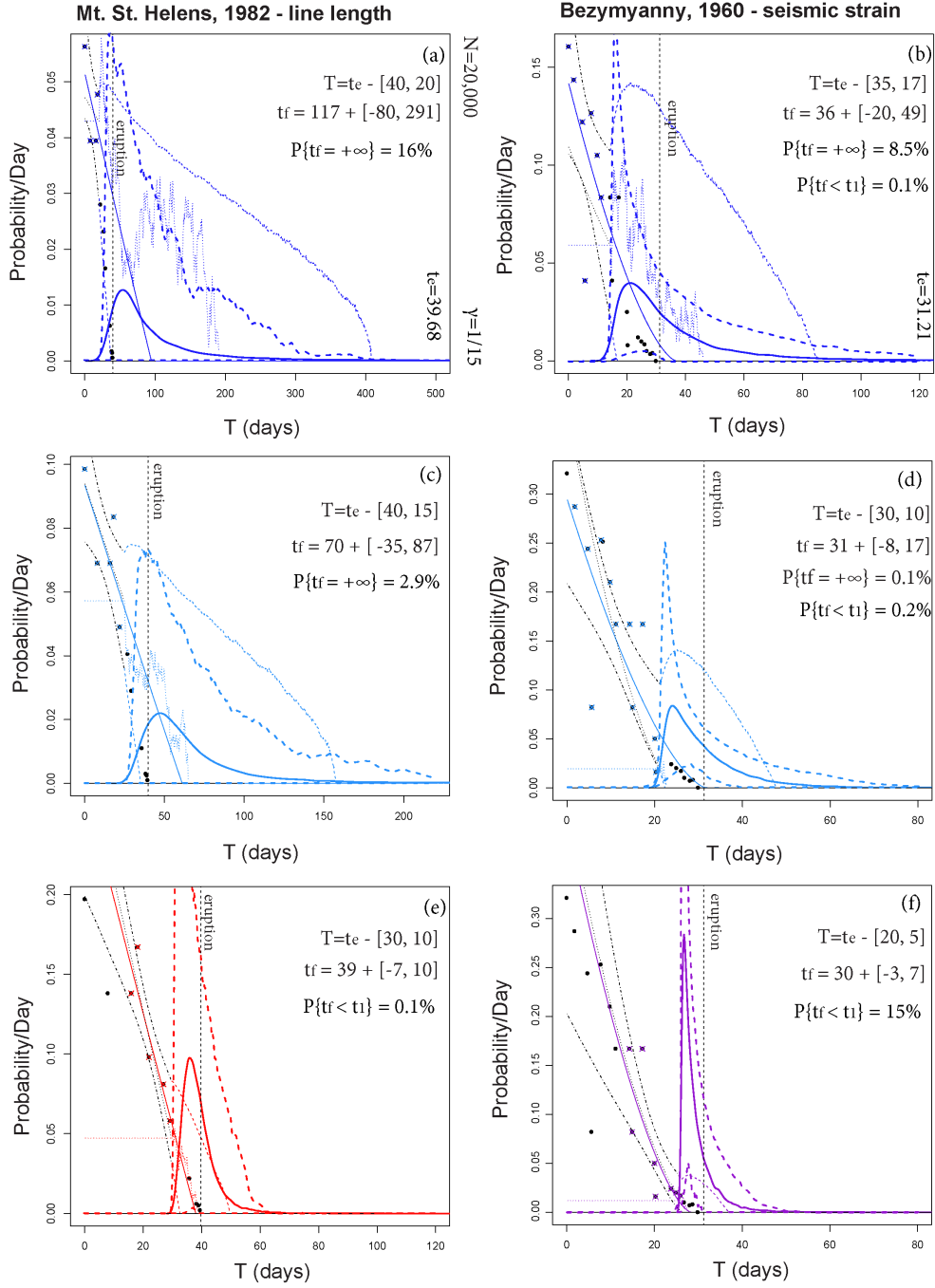


Figure 9: Forecasts of t_f based on Method 3. In (a,c,e) and (b,d,f) two examples are tested on three different time windows T . The bold line is g_{t_f} , and bold dashed lines are its 5th and 95th percentile values. Thin dashed lines bound the 90% confidence interval of the SDE paths, and a thin continuous line is the mean path. Thin dotted lines show examples of random paths. A thin dashed line marks $1/x_0$, and a dashed black line marks t_e .

7 Discussion

We described three different methods for estimating t_f , the ODE-based Method 1, the new SDE-based Method 2, and its doubly stochastic formulation Method 3. We tested the methods on six case studies, and in two of them we also performed forecasts on moving time windows. Figure 10 summarizes the material failure likelihood in the t_e day of the six case studies, reported as a probability percentage. Plot (a) compares Method 1 (black bars) and Method 2 (colored bars). Method 1 always outperforms Method 2 when α is based on the more accurate HT (red bars), and provides likelihoods above 15% in four cases over five. In contrast, when α is based on LLT (blue bars) the two methods provide similar likelihoods, below 5% in four cases over five, and below 1% in two cases. Plot (b) displays the likelihood provided by the doubly stochastic Method 3. Full colored bars report the mean likelihood, shaded bars the 95th percentiles of the likelihood. Mean likelihoods are very similar to those provided by Method 2, but when those were below 1%, these are $\approx 1\%$. The 95th percentile values are significantly higher. In particular, when α is based on LLT (blue bars), Method 3 percentiles are all higher than the Method 1 values.

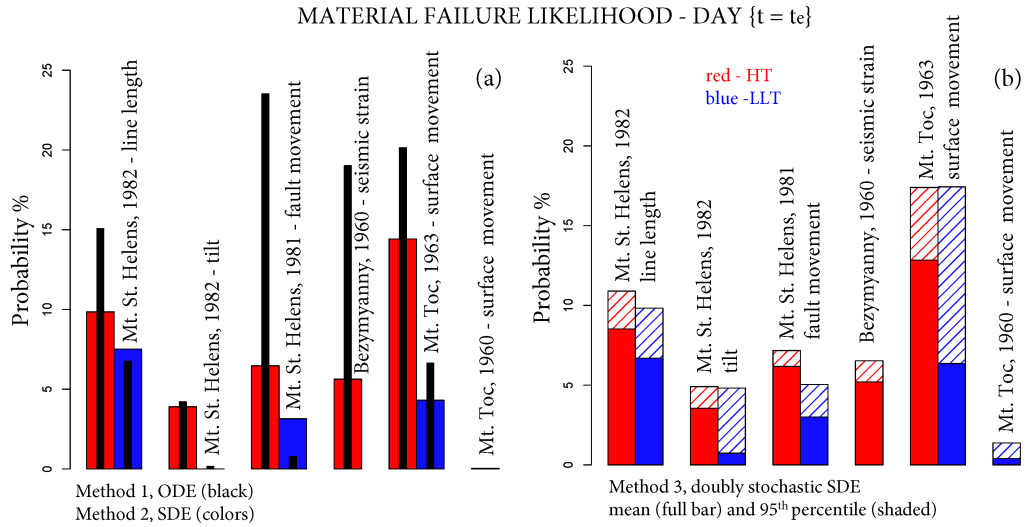


Figure 10: Barplots of the likelihood $P\{t_e = t_f\}$. In plot (a) the black bars assume Method 1, the colored bars Method 2. Plot (b) assumes Method 3, and the full bars are the mean values, and the shaded bars are the 95th percentile values of the likelihood.

This features are confirmed and strengthened in the material failure likelihoods of the forecasting examples based on the moving windows. Figure 11 summarizes these likelihoods. Plot (a) compares Method 1 (black bars) and Method 2 (colored bars). In Mt. St. Helens, 1982 - line length (blue), Method 2 outperforms Method 1 only in the third time window, and it is the only likelihood above 10%. In Bezmyanny, 1960 - seismic strain (red), Method 2 outperforms Method 1 only in the first time window, and the likelihoods are all close to 5%. Plot (b) displays the likelihoods provided by the doubly stochastic Method 3. Full colored bars report the mean likelihood, shaded bars its 95th percentile values. In this case, mean likelihoods are very similar to those provided by Method 1, but slightly lower. The 95th percentile values are again significantly higher, around 5% in the first and second time windows, and about 16% and 12% in the Mt. St. Helens and Bezmyanny case studies, respectively.

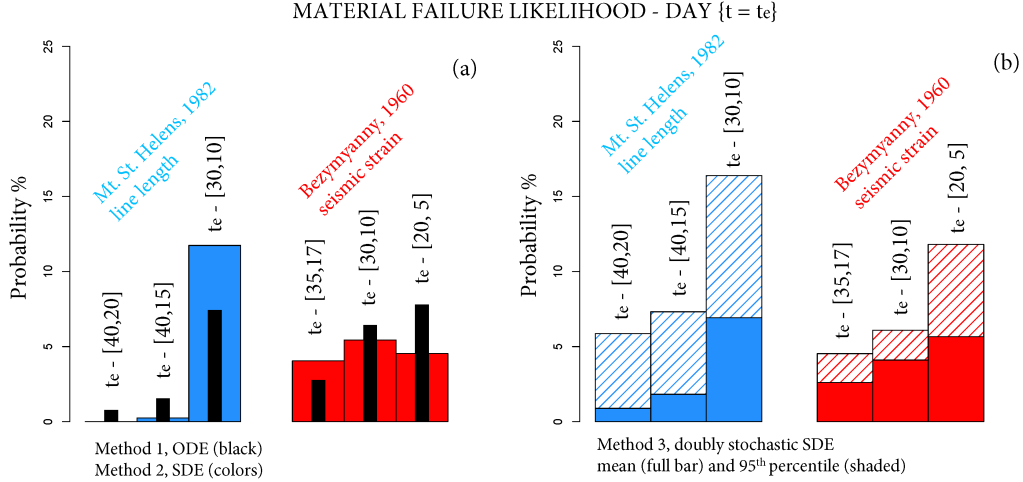


Figure 11: Barplots of the likelihood $P\{t_e = t_f\}$ in two forecasting examples, on three different time windows. In plot (a) the black bars assume Method 1, the colored bars Method 2. Plot (b) assumes Method 3, and the full bars are the mean values, and the shaded bars are the 95th percentile values of the likelihood.

8 Conclusions

In this study, we have introduced a new doubly stochastic method for performing material failure forecasts. The method enhances the well known FFM equation, introducing a new formulation similar to the Hull-White model. The model is a mean-reverting SDE, which assumes the traditional ODE as the mean solution. New parameters include the noise standard deviation σ and the mean-reversion rapidity γ . They are estimated based on the properties of the residuals in the original linearized problem. The implementation allows the model to make excursions from the classical solutions, including the possibility of some degree of aleatory uncertainty in the estimation. This provides probability forecasts instead that deterministic predictions.

We compared the new method and the forecasting method based on the classical formulation. We also compared an Hull-White model without considering the model uncertainty, and its doubly stochastic formulation. A comparison is performed on six historical datasets of precursory signals already studied with the classical FFM, including tilt, line-length, and fault movement at Mt. St. Helens, 1981-82, seismic signals registered from Bezymyanny, 1960, and surface movement of Mt. Toc, 1960-63. We also considered forecasting problems over moving time windows, based on data in the case studies of Mt. St. Helens, 1982 and Bezymyanny, 1960. The data shows the performance of the methods across a wide range of possible values of convexity α and amounts of scattering in the observations, and the increased forecasting skill of the doubly stochastic formulation in Method 3.

The doubly stochastic formulation is particularly impacting in the forecasts because it enables the calculation of the 95th percentiles of the probability of failure. This values are generally higher than the mean estimates, and represent the *worst case scenario* with a probability of occurrence above 5%. This was not possible in the classical formulation. This approach is the subject of ongoing and future work, with the purpose to further enhance the short-term eruption forecasting robustness.

Acknowledgements

We would like to thank Barry Voight for helpful discussions and inspiration. We would also like to acknowledge the support of NSF awards 1521855, 1621853, and 1339765.

A Classical statistical analysis of FFM

In the ODE problem, regressive models can be applied on different formulations of the differential equation. Even if these formulations are algebraically equivalent, the result of the regression can change significantly. We describe three different methods reported in Voight (1988a), and then fully detailed in Cornelius and Voight (1995). We follow the notation of Cornelius and Voight (1995). Nonlinear regression methods have also been developed, but in this study we relied on the linearized method for simplicity (Bell et al., 2011).

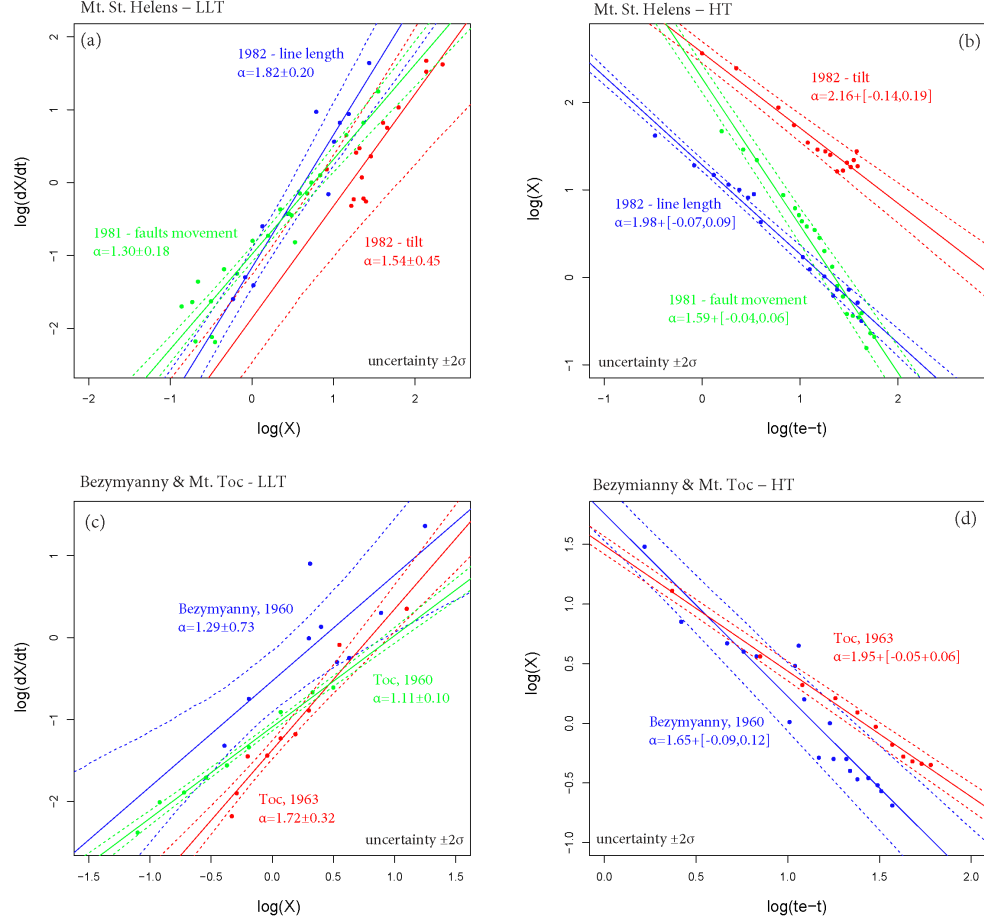


Figure 12: Methods LLT and HT applied to (a,b) St. Helens and (c,d) Bezymianny&Mt. Toc datasets. Different colors correspond to different data. Dashed lines bound the 90% confidence interval of the regression line. Figure modified from Voight (1988a).

Log-rate versus log-acceleration technique (LLT) The application of a linear regressive model (LRM) on the equation (from eq. 1):

$$\log\left(\frac{dX}{dt}\right) = \alpha \log(X) + \log(A)$$

can produce estimates of α and $\log(A)$. It requires an approximation to the rate change, which typically suffers of data scattering. Then, A is not robustly constrained by its logarithm. Moreover, the equation may be not well-posed in case of negative rates, requiring to neglect some values, or to apply the equation to $X + c > 0$.

Hindsight technique (HT) A LRM can be applied to the equation (from eq. 3, with $t_0 = t_f$):

$$\log(X(t)) = \frac{1}{1-\alpha} \log(t_f - t) + \frac{\log[A(\alpha-1)]}{1-\alpha},$$

producing estimates of $\frac{1}{1-\alpha}$ and $\frac{\log[A(\alpha-1)]}{1-\alpha}$. It does not rely on the rate change, but requires to know the failure time t_f in advance. This is the reason of its name. Thus, it is not a method producing forecasts, but can be solely used in hindcasting problems. Moreover, while the value of α is well constrained, the value of A is not. The uncertainty range affecting A is increased by the uncertainty affecting α , and the estimate is done in logarithmic scale.

Linearized least-squares method (LLSM) Finally, a LRM can be applied to eq. 2:

$$X(t)^{1-\alpha} = (1-\alpha)A(t-t_0) + \eta(t_0),$$

producing estimates of $(1-\alpha)A$ and $\hat{\eta}(t_0)$. It does not rely on the rate change or on the failure time, but requires an estimate of α from another method, or an iterative approximation possibly based on nonlinear regression.

Figure 12 shows the results of the LLT and HT applied to the Mt. St. Helens (a,b), and to the Bezymyanny & Mt. Toc datasets (c,d). We note that the accuracy of HT is generally higher. In detail, the Mt. St. Helens tilt dataset shows significantly discordant results between LLT and HT. This is motivated by the great scattering in the initial measurements, and discarding the first ten points increases accuracy. The uncertainty affecting α in the Bezymyanny dataset according to LLT is very large and only HT is implemented in our examples. The HT results of the Mt. Toc, 1960 dataset were not provided in the original study.

B Sensitivity analysis on the noise properties

Discrete observations provide us information on $K = \frac{\sigma^2}{\gamma}$, which is the variance of the solution of the Ornstein-Uhlenbeck process associated to our SDE. However, solutions with the same K can look significantly different, as shown in Figure 3b.

The estimators in all our case studies assume $\gamma = 1/15$. This is a choice based on the empirical observation that the total length of temporal sequence is at the scale of 45 days, and the duration of well-aligned observations is at the scale of 15 days. In Figure 13 we show examples of solutions with doubled or halved γ . There is an apparent effect on the 90% confidence interval of the SDE paths, which is enlarged increasing γ , and terminally bent down towards the real axis. However, the effect of g_{t_f} is minor, and increasing γ of four times reduces $E[t_f]$ of about 5 days.

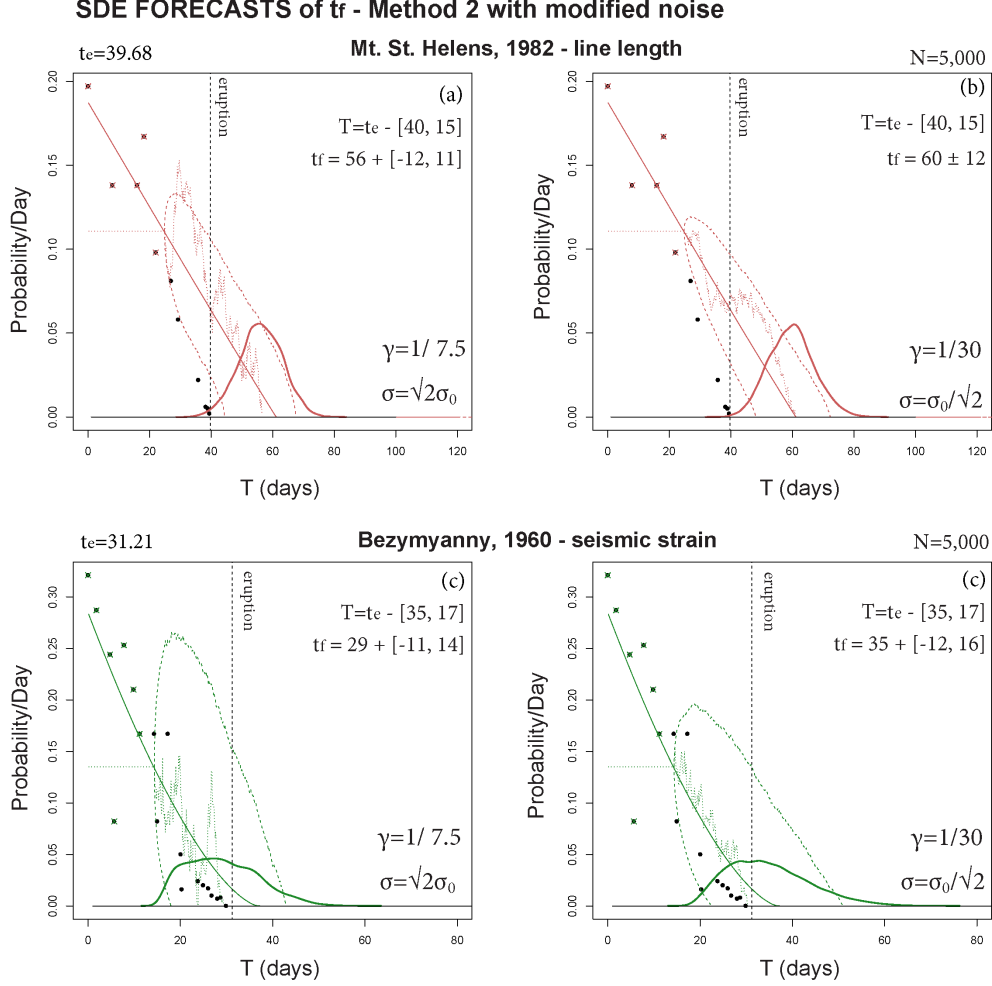


Figure 13: Forecasts of t_f based on Method 2. The solutions assume equal $K = \frac{\sigma^2}{\gamma}$, but different (σ, γ) . In plots (a,c) $\gamma^{-1} = 7.5$, and in plots (b,d) $\gamma^{-1} = 30$. The bold line is the pdf of t_f . Thin dashed lines bound the 90% confidence interval of the SDE paths, and a thin continuous line is the median path. Thin dotted lines show examples of random paths. A thin dashed line marks $1/x_0$, and a dashed black line marks t_e .

References

- Bebbington, M. S. (2013). Assessing spatio-temporal eruption forecasts in a monogenetic volcanic field. *Journal of Volcanology and Geothermal Research*, 252(Supplement C):14 – 28.
- Bell, A. F., Naylor, M., Heap, M. J., and Main, I. G. (2011). Forecasting volcanic eruptions and other material failure phenomena: An evaluation of the failure forecast method. *Geophysical Research Letters*, 38(15):5.
- Bevilacqua, A. (2016). *Doubly stochastic models for volcanic hazard assessment at Campi Flegrei caldera*, volume 21 of *Theses*. Birkhäuser/Springer.
- Bevilacqua, A., Bursik, M., Patra, A., Pitman, E., Qingyuan, Y., Sangani, R., and Kobs-Nawotniak, S. (2018). Late Quaternary eruption record and probability of future volcanic eruptions in the

- Long Valley volcanic region (CA, USA). *Journal of Geophysical Research: Solid Earth*, in press. doi:10.1002/2018JB015644.
- Bevilacqua, A., Flandoli, F., Neri, A., Isaia, R., and Vitale, S. (2016). Temporal models for the episodic volcanism of Campi Flegrei caldera (Italy) with uncertainty quantification. *Journal of Geophysical Research: Solid Earth*, 121(11):7821–7845.
- Bevilacqua, A., Isaia, R., Neri, A., Vitale, S., Aspinall, W. P., Bisson, M., Flandoli, F., Baxter, P. J., Bertagnini, A., Esposti Ongaro, T., Iannuzzi, E., Pistolesi, M., and Rosi, M. (2015). Quantifying volcanic hazard at Campi Flegrei caldera (Italy) with uncertainty assessment: 1. Vent opening maps. *Journal of Geophysical Research: Solid Earth*, 120(4):2309–2329.
- Bevilacqua, A., Marcus, B., Abani, P., E. Bruce, P., and Ryan, T. (2017a). Bayesian construction of a long-term vent opening map in the Long Valley volcanic region, (CA, USA). *Statistics in Volcanology*, 3(1):1–36.
- Bevilacqua, A., Neri, A., Bisson, M., Esposti Ongaro, T., Flandoli, F., Isaia, R., Rosi, M., and Vitale, S. (2017b). The effects of vent location, event scale, and time forecasts on pyroclastic density current hazard maps at Campi Flegrei caldera (Italy). *Frontiers in Earth Science*, 5:72.
- Chiodini, G., Paonita, A., Aiuppa, A., Costa, A., Caliro, S., De Martino, P., Acocella, V., and Vande-meulebrouck, J. (2016). Magmas near the critical degassing pressure drive volcanic unrest towards a critical state. *Nature Communications*, 7:1–9.
- Cornelius, R. and Voight, B. (1994). Seismological aspects of the 1989-1990 eruption at Redoubt Volcano, Alaska: the Materials Failure Forecast Method (FFM) with RSAM and SSAM seismic data. *Journal of Volcanology and Geothermal Research*, 62:469–498.
- Cornelius, R. and Voight, B. (1995). Graphical and PC-software analysis of volcano eruption precursors according to the Material Failure Forecast Method (FFM). *Journal of Volcanology and Geothermal Research*, 64:295–320.
- Cornelius, R. and Voight, B. (1996). Real time seismic amplitude measurement (RSAM) and seismic spectral amplitude measurement (SSAM) analyses with the material failure forecast method (FFM), June 1991 explosive eruption at Mount Pinatubo. In *Geophysical Unrest*.
- Hull, J. and White, A. (1990). Pricing Interest Rate Derivatives Securities. *The Review of Financial Studies*, 3:573–592.
- Kilburn, C. R. (2003). Multiscale fracturing as a key to forecasting volcanic eruptions. *Journal of Volcanology and Geothermal Research*, 125(3):271 – 289.
- Kilburn, C. R. J. and Voight, B. (1998). Slow rock fracture as eruption precursor at Soufriere Hills Volcano, Montserrat. *Geophysical Research Letters*, 25(19):3665–3668.
- Marzocchi, W. and Bebbington, M. S. (2012). Probabilistic eruption forecasting at short and long time scales. *Bulletin of Volcanology*, 74(8):1777–1805.
- Neri, A., Bevilacqua, A., Esposti Ongaro, T., Isaia, R., Aspinall, W. P., Bisson, M., Flandoli, F., Baxter, P. J., Bertagnini, A., Iannuzzi, E., Orsucci, S., Pistolesi, M., Rosi, M., and Vitale, S. (2015). Quantifying volcanic hazard at Campi Flegrei caldera (Italy) with uncertainty assessment: 2. Pyroclastic density current invasion maps. *Journal of Geophysical Research: Solid Earth*, 120(4):2330–2349.
- Ortiz, R., Moreno, H., García, A., Fuentealba, G., Astiz, M., Pena, P., Sánchez, N., and Tárrega, M. (2003). Villarrica volcano (Chile): characteristics of the volcanic tremor and forecasting of small explosions by means of a material failure method. *Journal of Volcanology and Geothermal Research*, 128(1):247 – 259.
- Richardson, J., Wilson, J., Connor, C., Bleacher, J., and Kiyosugi, K. (2017). Recurrence rate and magma effusion rate for the latest volcanism on Arsia Mons, Mars. *Earth and Planetary Science Letters*, 458:170–178.

- Selva, J., Orsi, G., Di Vito, M. A., Marzocchi, W., and Sandri, L. (2012). Probability hazard map for future vent opening at the Campi Flegrei caldera, Italy. *Bulletin of Volcanology*, 74(2):497–510.
- Smith, R. and Kilburn, C. (2010). Forecasting eruptions after long repose intervals from accelerating rates of rock fracture: The June 1991 eruption of Mount Pinatubo, Philippines. *Journal of Volcanology and Geothermal Research*, 191(1):129 – 136.
- Smith, R., Sammonds, P. R., and Kilburn, C. R. (2009). Fracturing of volcanic systems: Experimental insights into pre-eruptive conditions. *Earth and Planetary Science Letters*, 280(1):211 – 219.
- Sparks, R. and Aspinall, W. (2004). *Volcanic activity: frontiers and challenges in forecasting, prediction and risk assessment*, volume 19 of *Geophysical Monograph 150*, pages 359–373. IUGG.
- Tadini, A., Bevilacqua, A., Neri, A., Cioni, R., Aspinall, W. P., Bisson, M., Isaia, R., Mazzarini, F., Valentine, G. A., Vitale, S., Baxter, P. J., Bertagnini, A., Cerminara, M., de Michieli Vitturi, M., Di Roberto, A., Engwell, S., Esposti Ongaro, T., Flandoli, F., and Pistolesi, M. (2017a). Assessing future vent opening locations at the Somma-Vesuvio volcanic complex: 2. Probability maps of the caldera for a future Plinian/sub-Plinian event with uncertainty quantification. *Journal of Geophysical Research: Solid Earth*, 122(6):4357–4376.
- Tadini, A., Bisson, M., Neri, A., Cioni, R., Bevilacqua, A., and Aspinall, W. P. (2017b). Assessing future vent opening locations at the Somma-Vesuvio volcanic complex: 1. A new information geodatabase with uncertainty characterizations. *Journal of Geophysical Research: Solid Earth*, 122(6):4336–4356.
- Voight, B. (1987). Phenomenological law enables accurate time forecasts of slope failure. In *Int. Soc. Rock Mechanics, 7th International Congress of Rock Mechanics, Montreal*.
- Voight, B. (1988a). A method for prediction of volcanic eruptions. *Nature*, 332:125–130.
- Voight, B. (1988b). Material science law applies to time forecasts of slope failure. In *5th International Symposium on Landslides, Lausanne*.
- Voight, B. (1989). A relation to describe rate-dependent material failure. *Science*, 243(4888):200–203.
- Voight, B. and Cornelius, R. R. (1991). Prospects for eruption prediction in near real-time. *Nature*, 350:695–698.
- Voight, B., Orkan, N., and Young, K. (1989). Deformation and failure-time prediction in rock mechanics. In *Rock Mechanics as a Guide for Efficient Utilization of Natural Resources*.
- Voight, B., Young, K., Hidayat, D., Subandrio, Purbawinata, M., Ratdomopurbo, A., Suharna, Panut, Sayudi, D., LaHusen, R., Marso, J., Murray, T., Dejean, M., Iguchi, M., and Ishihara, K. (2000). Deformation and seismic precursors to dome-collapse and fountain-collapse nuées ardentes at Merapi Volcano, Java, Indonesia, 1994-1998. *Journal of Volcanology and Geothermal Research*, 100(1):261 – 287.